Supplement of

Heterogeneous Nitrosation Reactions of Amines Driven by Dinitrogen Tetroxide: A Missing Source of Particulate Nitrosamines

Tai-Xing Chi et al.

Correspondence to: Feng-Yang Bai (baify492@nenu.edu.cn) and Xiu-Hui Zhang (zhangxiuhui@bit.edu.cn)

Table of Contents

Figure S6. The representative temperature and potential energy profile of MA equilibration at the droplet interface during NVT-ensemble BOMD simulations at 300 K. The calculated mean values and standard deviations of both temperature and potential energy confirm the MA has reached equilibrium at the droplet interface by 10 ps.

Figure S7. Optimized molecular structure (bond lengths in Å) and calculated Mayer bond orders (in brackets) of *t*-$ONONO_2$, obtained at the B3LYP-D3/6-311++G(3df,2p) level of theory.

Figure S8. Interaction region indicator (IRI) analysis of *t*-$ONONO_2$. **(a)** Two-dimensional scatter plots, sign(λ_2)ρ vs IRI; **(b)** sign(λ_2)ρ-mapped isosurface of IRI = 1.0. Sign(λ_2) indicates the sign of the second largest eigenvalue λ_2 of the electron density (ρ) Hessian matrix. The values of ρ correlate positively with the bond strength. The employed wave function was calculated at the B3LYP-D3/6-311++G(3df,2p) level of theory.

Figure S9. The representative temperature and potential energy profile of DMA equilibration at the droplet interface during NVT-ensemble BOMD simulations at 300 K. The calculated mean values and standard deviations of both temperature and potential energy confirm the DMA has reached equilibrium at the droplet interface by 8 ps.

Figure S10. Time evolution of key bond distances mediated by MA and DMA. **(a)** MA-mediated, two water bridge; **(b)** MA-mediated, three water bridge; **(c)** DMA-mediated, one water bridge; **(d)** DMA-mediated, two water bridge. The green arrows denote atom transfer directions, while the dashed lines represent intermolecular interactions.

Figure S11. The interaction region indicator (IRI) analysis of interfacial reaction products on the nanodroplet surface: **(a)** NO_3^- + MAH^+ + HONO (on the droplet) and **(b)** NO_3^- + $DMAH^+$ + HONO (on the droplet) . The ρ represents the electron density, and sign(λ_2) denotes the sign of the second largest eigenvalue of the Hessian of ρ. The purple, red, white, and cyan spheres represent the N, O, H, and C atoms, respectively.

Figure S12. Potential energy surface for the reaction of *t*-HONO with DMA (unit: kcal mol^{-1}) at the CCSD(T)/aug-cc-pVTZ//B3LYP-D3/6-311++G(3df,2p) level of theory in the gas phase (g) and aqueous phase (aq). The data in parentheses are the corresponding bond lengths in the aqueous solution. The bond lengths are in angstroms (Å). The red, blue, white, and silver spheres represent O, N, H and C atoms, respectively.

Figure S13. Collective variable (CV) for the metadynamics (MetaD) simulations. The CV tracks the formation (blue) and breaking (red) of all relevant bonds occurring during the N-nitrosation reaction of DMA with HONO at the air–water interface. For MetaD simulations, the CV was defined as: d_{CV} = d1 +

d2 − d3 − d4.

Figure S14. Convergence analysis of MetaD simulations for the N-nitrosation reaction between DMA and HONO at the air–water interface, based on the time evolution of the CV.

Table S1. Calculated frequencies (cm^{-1}) of the reactants, products, transition states and complexes at the B3LYP-D3/6-311++G(3df,2p) level of theory (g: gas phase; aq: aqueous phase simulated with the SMD model).

Supplementary Methods

Section S1. Unbiased BOMD simulations.

The unbiased BOMD simulations were performed to demonstrate that the N-nitrosation reactions of MA/DMA with N_2O_4 and the hydrolysis of *t*-$ONONO_2$ mediated by MA and DMA can occur rapidly. The simulation system was fully relaxed to reach statistical equilibrium (Fig. S2). Subsequent simulations confirmed that the above reactions proceed rapidly and spontaneously under equilibrium conditions.

Section S2. Well-tempered metadynamics simulations.

To probe the reaction barriers between HONO and DMA at the air−water interface, metadynamics (MetaD) simulations were carried out. The collective variable (CV), a key parameter for enhanced sampling, was defined to clearly distinguish between reactant, transition, and product states (Fig. S13). The upper and lower bounds of the CV were determined based on the interfacial behavior observed in unbiased BOMD simulations. Gaussian hills with adaptive heights and width parameter σ of 0.3 Å were deposited every 30 steps to efficiently explore the free energy landscape and accelerate convergence (Fig. S14).

Section S3. Wave function analysis.

Using the optimized reactant structures and key intermediate structures from BOMD simulations, we performed wave function analysis based on density functional theory (DFT) calculations to elucidate the nature of intermolecular interactions.

S3.1 Structural and Mayer bond order (MBO) analysis of *t*-$ONONO_2$.

The optimized structure of *t*-$ONONO_2$ (Fig. S7) reveals five N–O covalent bonds, the longest being the N2–O3 bond at 1.623 Å. In addition, the Mayer bond order (MBO)(Mayer, 1983) values were computed for all N–O covalent bonds in *t*-$ONONO_2$. MBO reliability is well-established in various studies.(Mayer, 1983; Ning et al., 2024) Bond strength typically exhibits a positive correlation with bond order.

The calculated MBO for the N2–O3 covalent bond (0.641) is the lowest among all N–O bonds, confirming its weaker nature.

S3.2 Interaction region indicator (IRI) analysis.

The IRI analysis was employed to investigate the strength of localized interactions.(Lu and Chen, 2021) The derived IRI isosurfaces, color-mapped according to sign(λ_2)ρ values, characterize distinct interaction types including hydrogen bonding (HB) and covalent bonding. The term sign(λ_2) denotes the sign of the second-largest eigenvalue (λ_2) derived from the electron density Hessian matrix. Attractive interactions correspond to negative sign(λ_2) values, whereas positive values indicate repulsive interactions. The electron density (ρ) generally increases with interaction strength. As illustrated in Fig. S8, the N2–O3 covalent bond formed in *t*-$ONONO_2$ exhibits a spike sign(λ_2)ρ value of approximately −0.190 a.u. (the maximum value of ρ). IRI analysis indicates that the N2–O3 covalent bond exhibits the weakest interaction strength, making it more susceptible to cleavage than other N–O bonds in *t*-$ONONO_2$. This provides a mechanistic rationale for the spontaneous heterolysis of *t*-$ONONO_2$ to form the (NO_3^-)(NO^+) ion pair during equilibration at the air−water interface.

To further characterize intermolecular interactions, IRI analysis was carried out on the reaction products formed at the nanodroplet interface in BOMD simulations, and the results are presented in Fig. S11. In the IRI plots, blue regions indicate strong attractive interactions, such as ionic interactions (IB), hydrogen bonding (HB), and covalent bonds. Green areas correspond to van der Waals (vdW) interactions, while red zones denote repulsive interactions.

As shown in Fig. S11, distinct green regions appear between HONO and neighboring species, including NO_3^-, H_2O, MAH^+, and $DMAH^+$ (indicated by red

arrows), reflecting van der Waals interaction and HB.

Section S4. Interfacial reaction rate constant between DMA and HONO.

In this study, the rate constant k was calculated using transition state theory (TST), as given by the following expression:

$$k^{\mathrm{TST}} = \sigma \frac{k_B T}{h} e^{-\Delta G^{0,\neq}/(RT)}$$

where σ is the reaction path degeneracy, k_B is the Boltzmann constant, T is the absolute temperature (300 K), h is the Planck's constant, R is the molar gas constant, and $\Delta G^{0,\neq}$ denotes the Gibbs free energy barrier (the change in Gibbs free energy from reactants to the transition state). The calculated k^{TST} for the interfacial reaction between DMA and HONO is approximately 1.67×10^7 M^{-1} s^{-1}.

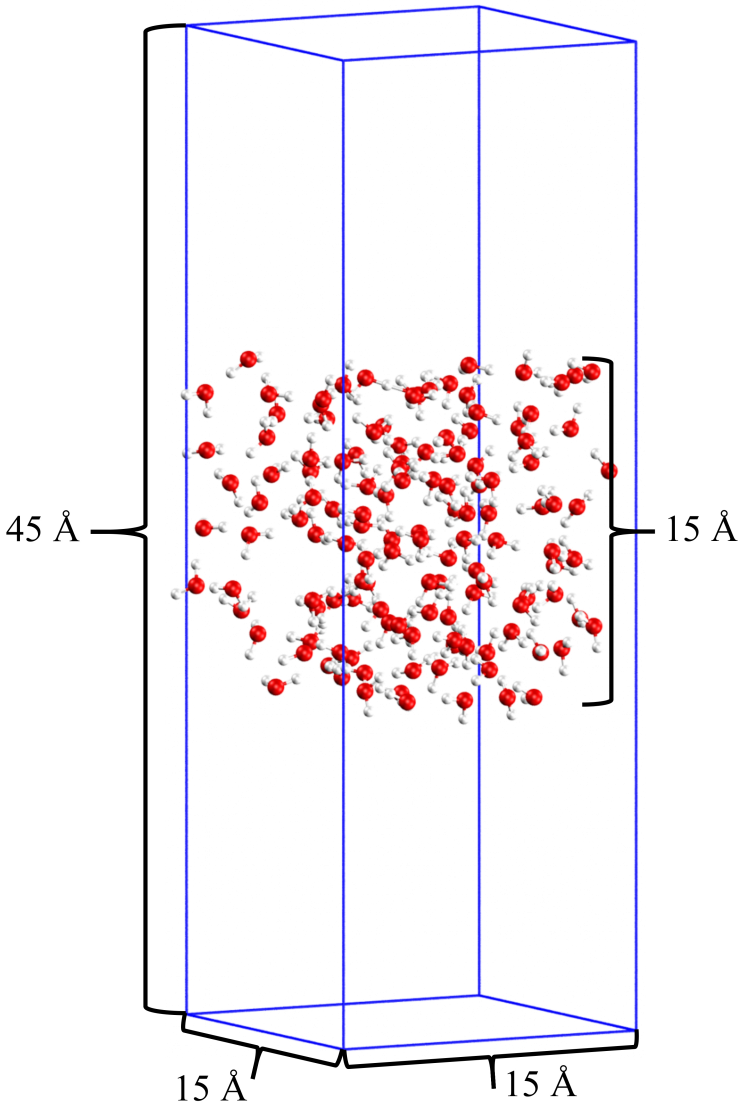

Figure S1. Model of the air–water interface. The simulation cell (15 Å × 15 Å × 45 Å) contains 128 water molecules, with a ~30 Å vacuum layer above a ~15 Å water slab along the *Z*-direction defining the interface.

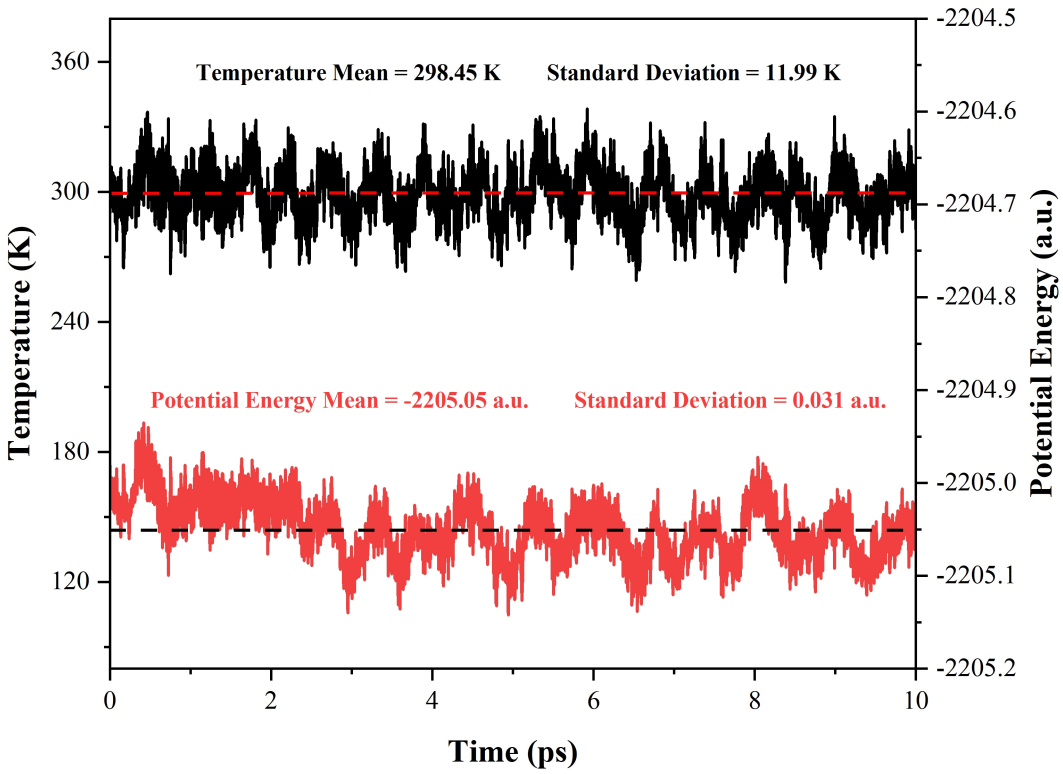

Figure S2. Evolution of temperature (black curve) and potential energy (black curve) during Born-Oppenheimer molecular dynamics (BOMD) simulations of the slab containing 128 water molecules in the NVT ensemble at 300 K. The corresponding averages are shown by horizontal lines (temperature: red; potential energy: black). The low standard deviations (energy: 0.001%; temperature: 4.02%) confirm the system reached equilibrium.

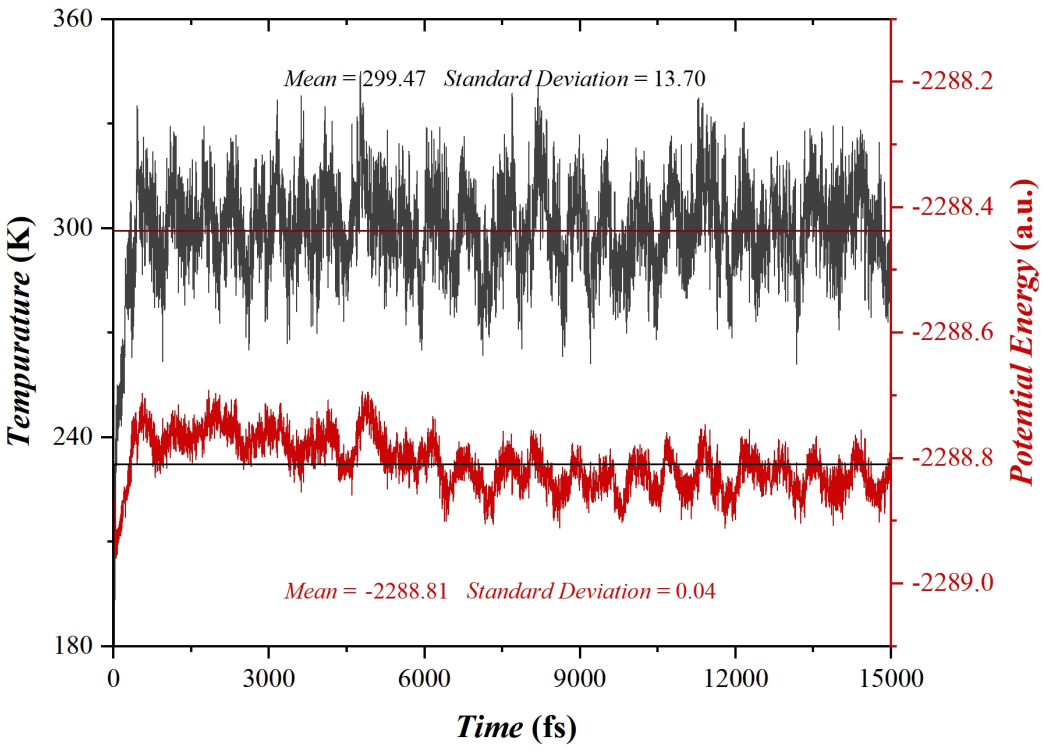

Figure S3. The representative temperature and potential energy profile of *t*-$ONONO_2$ equilibration at the droplet interface during NVT-ensemble BOMD simulations at 300 K. The calculated mean values and standard deviations of both temperature and potential energy confirm the *t*-$ONONO_2$ has reached equilibrium as the $(NO_3^-)(NO^+)$ ion pair at the droplet interface by 11.5 ps.

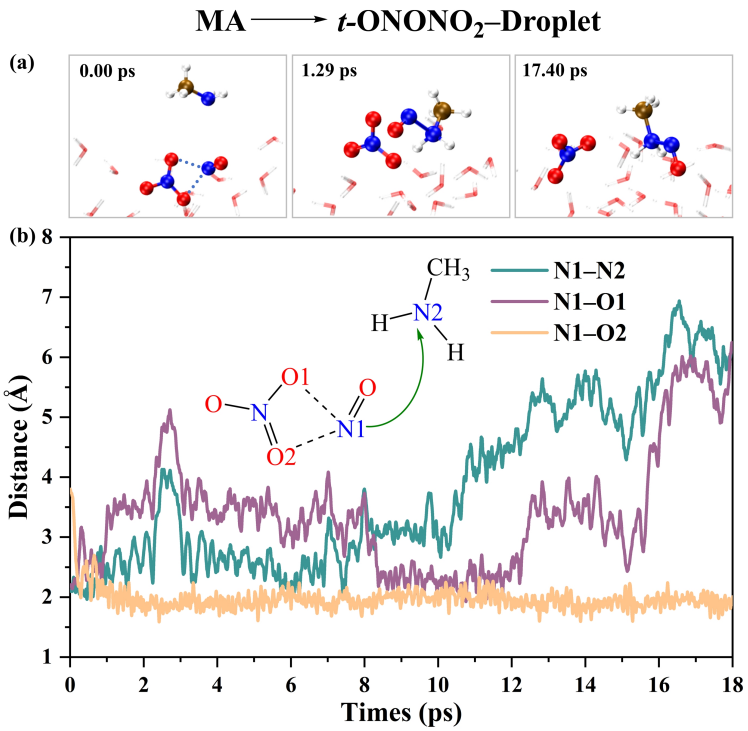

Figure S4. (a) Snapshot structures from the BOMD simulations, illustrating the stepwise mechanism of the MA-mediated N-nitrosation reaction of *t*-$ONONO_2$. **(b)** Time evolution of key bond distances mediated by MA. The black arrows indicate the directions of collision, while the dashed lines represent ionic bond. The blue, red, white, and ochre spheres represent the N, O, H, and C atoms, respectively. The green arrows denote atom transfer directions.

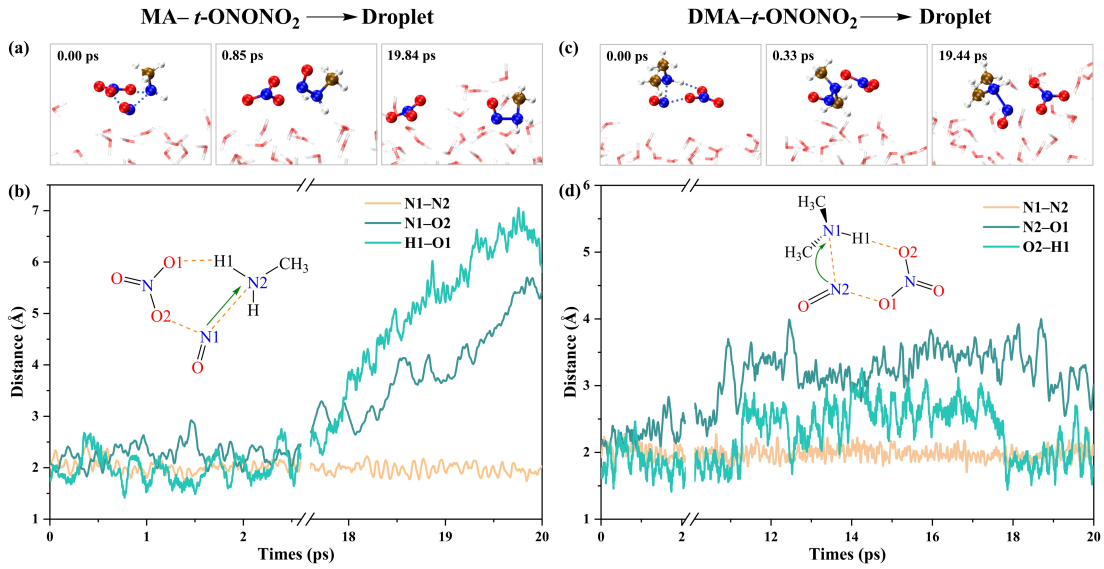

Figure S5. Snapshot structures from the BOMD simulations, illustrating the stepwise mechanism of the **(a)** MA- and **(c)** DMA-mediated N-nitrosation reaction of *t*-$ONONO_2$. Time evolution of key bond distances mediated by MA **(b)** and DMA **(d)**. The black arrows indicate the directions of collision, while the dashed lines represent ionic bond. The blue, red, white, and ochre spheres represent the N, O, H, and C atoms, respectively. The green arrows denote atom transfer directions.

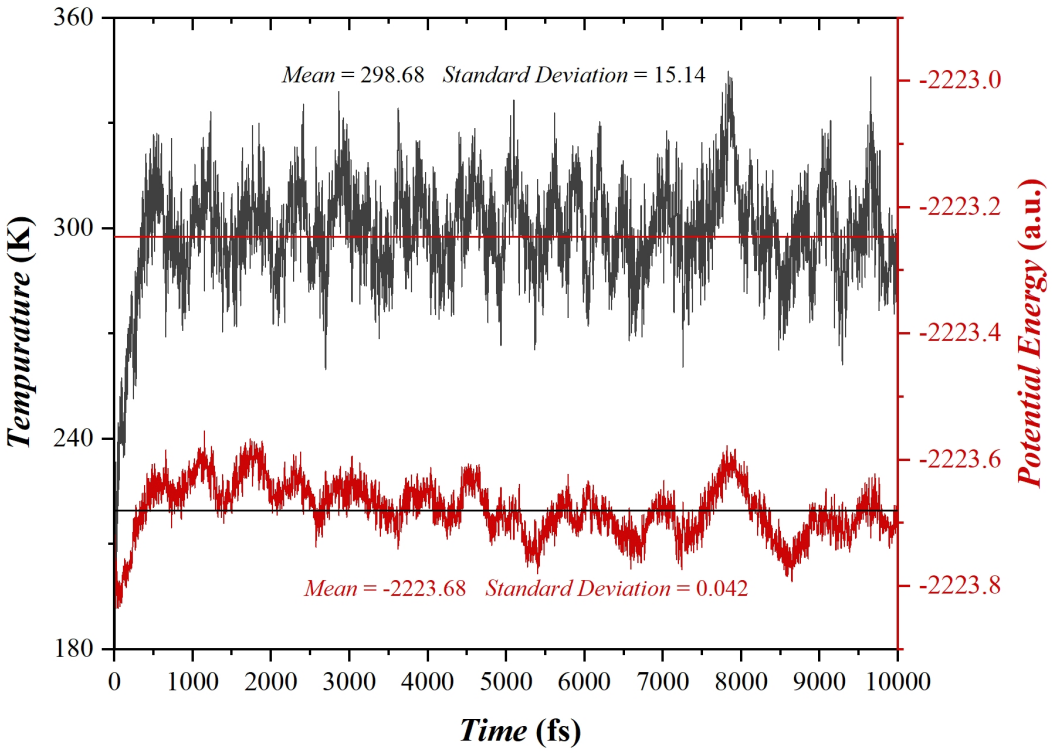

Figure S6. The representative temperature and potential energy profile of MA equilibration at the droplet interface during NVT-ensemble BOMD simulations at 300 K. The calculated mean values and standard deviations of both temperature and potential energy confirm the MA has reached equilibrium at the droplet interface by 10 ps.

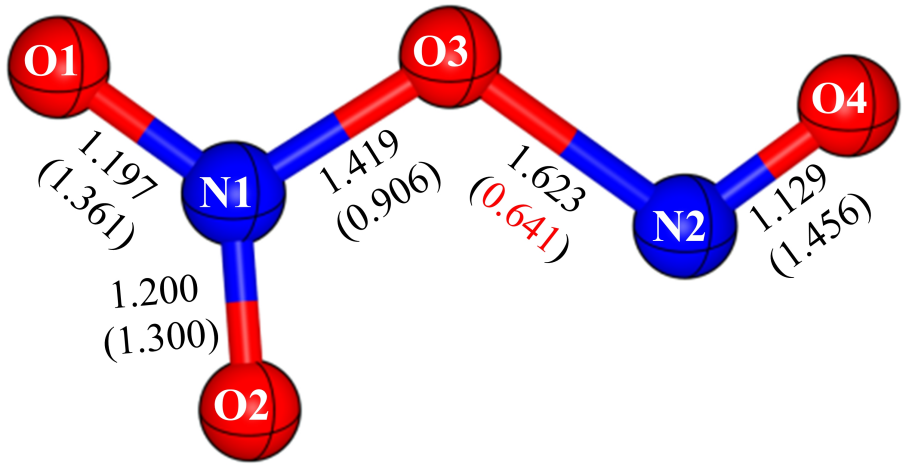

Figure S7. Optimized molecular structure (bond lengths in Å) and calculated Mayer bond orders (in brackets) of *t*-$ONONO_2$, obtained at the B3LYP-D3/6-311++G(3df,2p) level of theory.

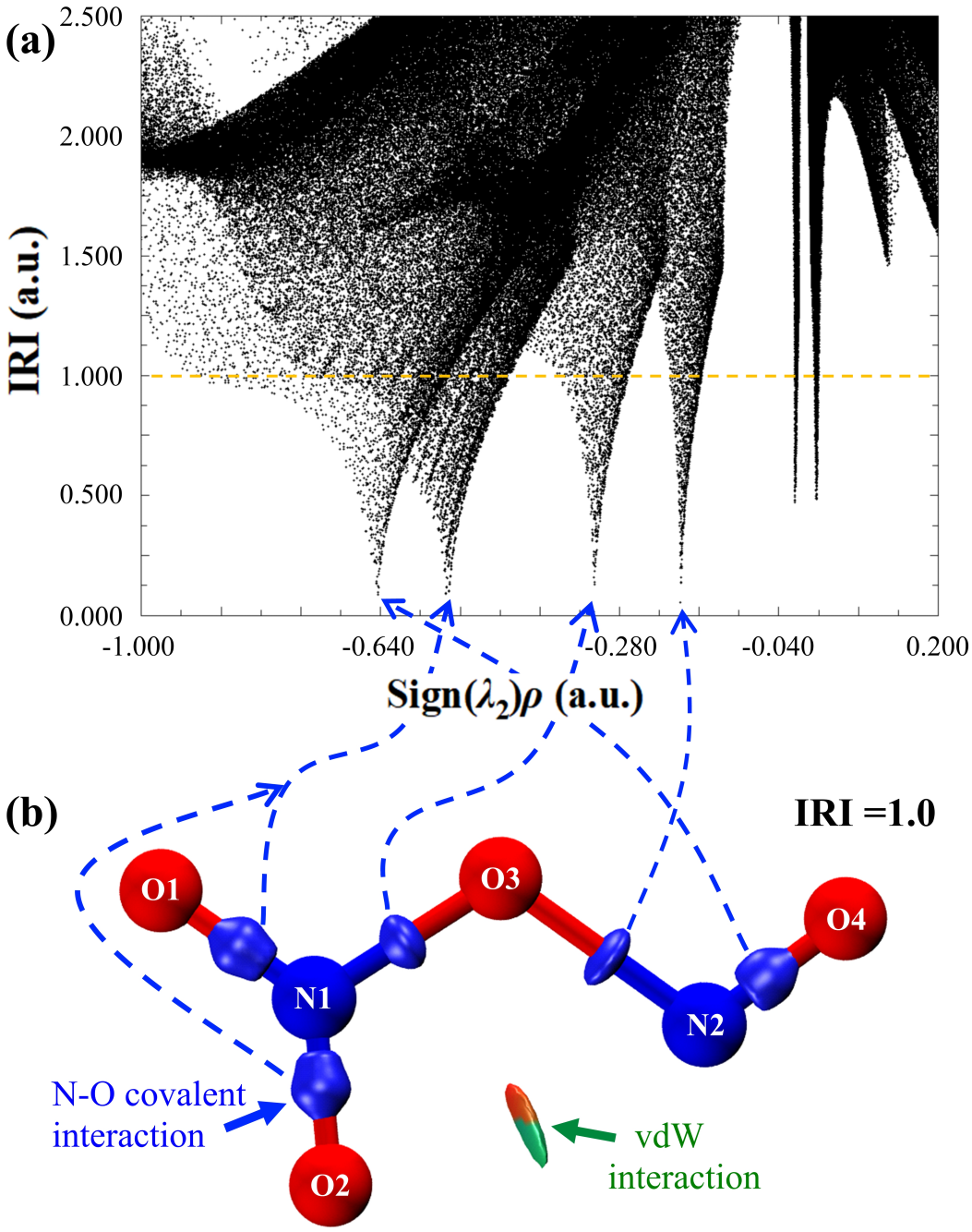

Figure S8. Interaction region indicator (IRI) analysis of *t*-ONONO$_2$. **(a)** Two-dimensional scatter plots, sign(λ_2)ρ vs IRI; **(b)** sign(λ_2)ρ-mapped isosurface of IRI = 1.0. Sign(λ_2) indicates the sign of the second largest eigenvalue λ_2 of the electron density (ρ) Hessian matrix. The values of ρ correlate positively with the bond strength. The employed wave function was calculated at the B3LYP-D3/6-311++G(3df,2p) level of theory.

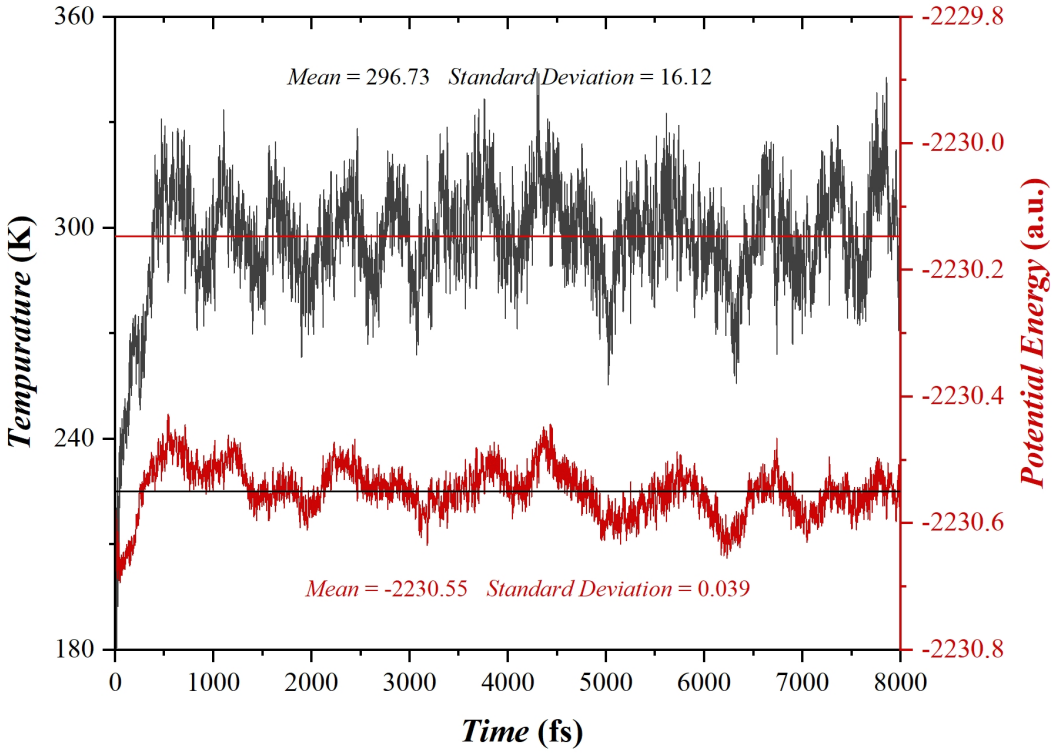

Figure S9. The representative temperature and potential energy profile of DMA equilibration at the droplet interface during NVT-ensemble BOMD simulations at 300 K. The calculated mean values and standard deviations of both temperature and potential energy confirm the DMA has reached equilibrium at the droplet interface by 8 ps.

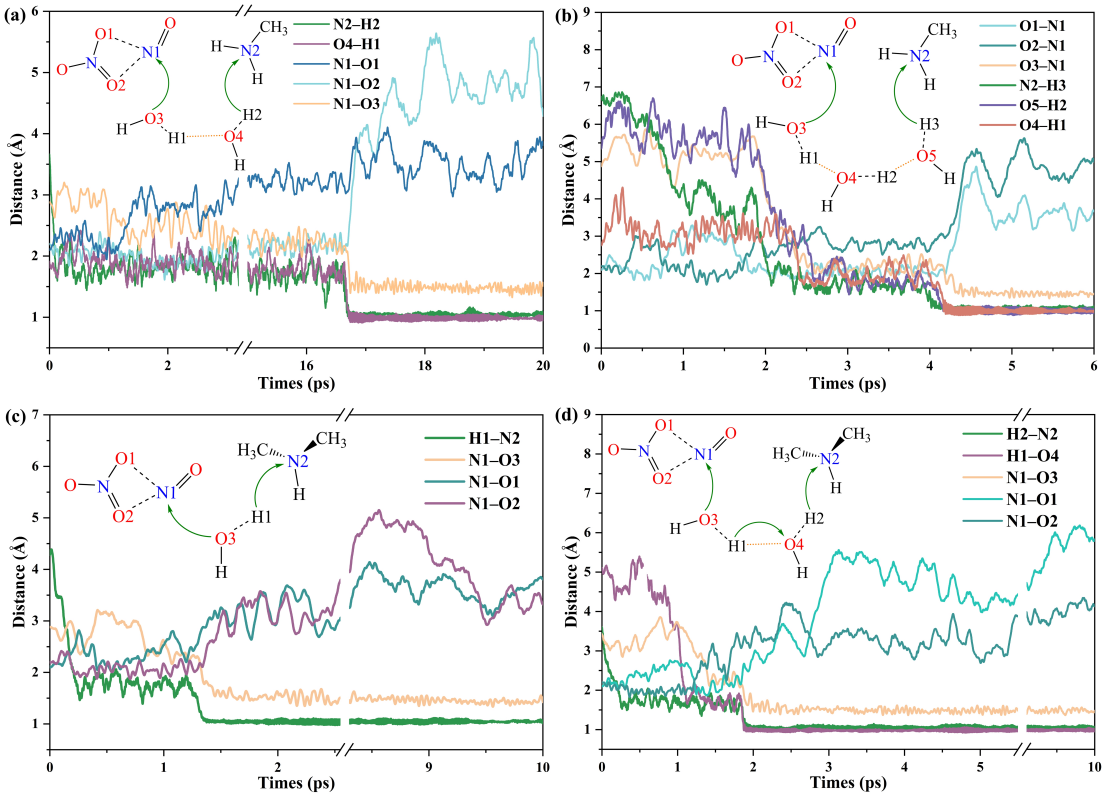

Figure S10. Time evolution of key bond distances mediated by MA and DMA. **(a)** MA-mediated, two water bridge; **(b)** MA-mediated, three water bridge; **(c)** DMA-mediated, one water bridge; **(d)** DMA-mediated, two water bridge. The green arrows denote atom transfer directions, while the dashed lines represent intermolecular interactions.

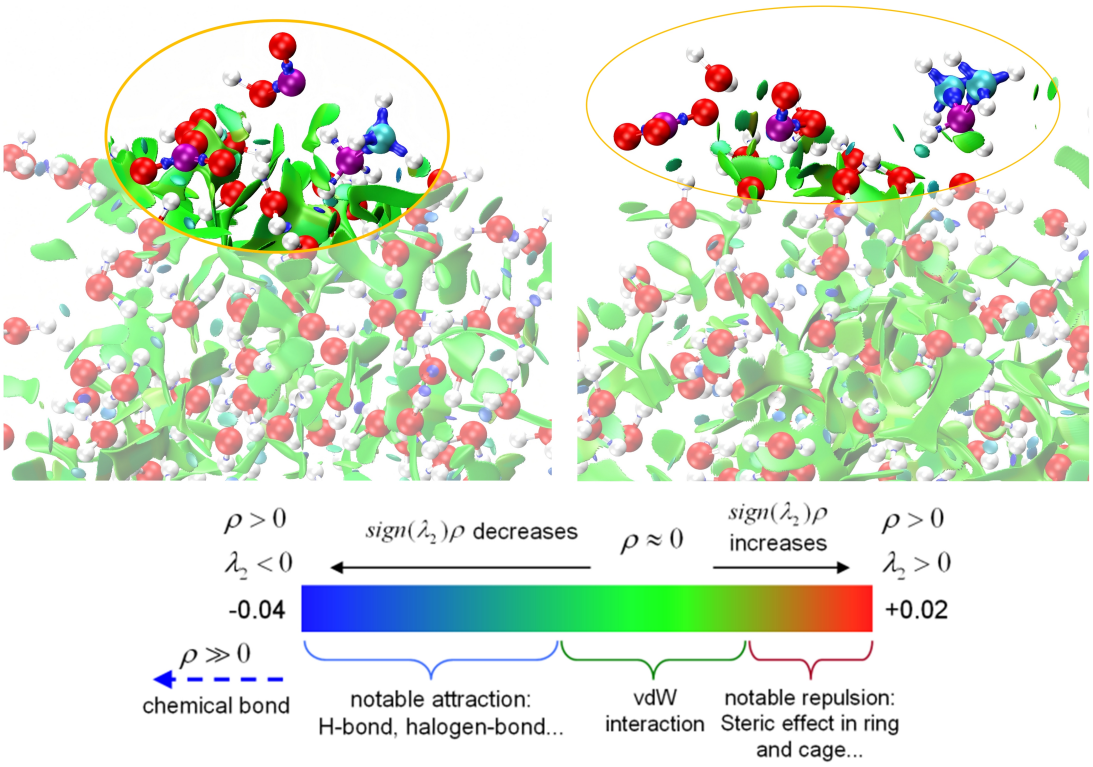

Figure S11. The interaction region indicator (IRI) analysis of interfacial reaction products on the nanodroplet surface: **(a)** NO_3^- + MAH^+ + HONO (on the droplet) and **(b)** NO_3^- + $DMAH^+$ + HONO (on the droplet). The ρ represents the electron density, and sign(λ_2) denotes the sign of the second largest eigenvalue of the Hessian of ρ. The purple, red, white, and cyan spheres represent the N, O, H, and C atoms, respectively.

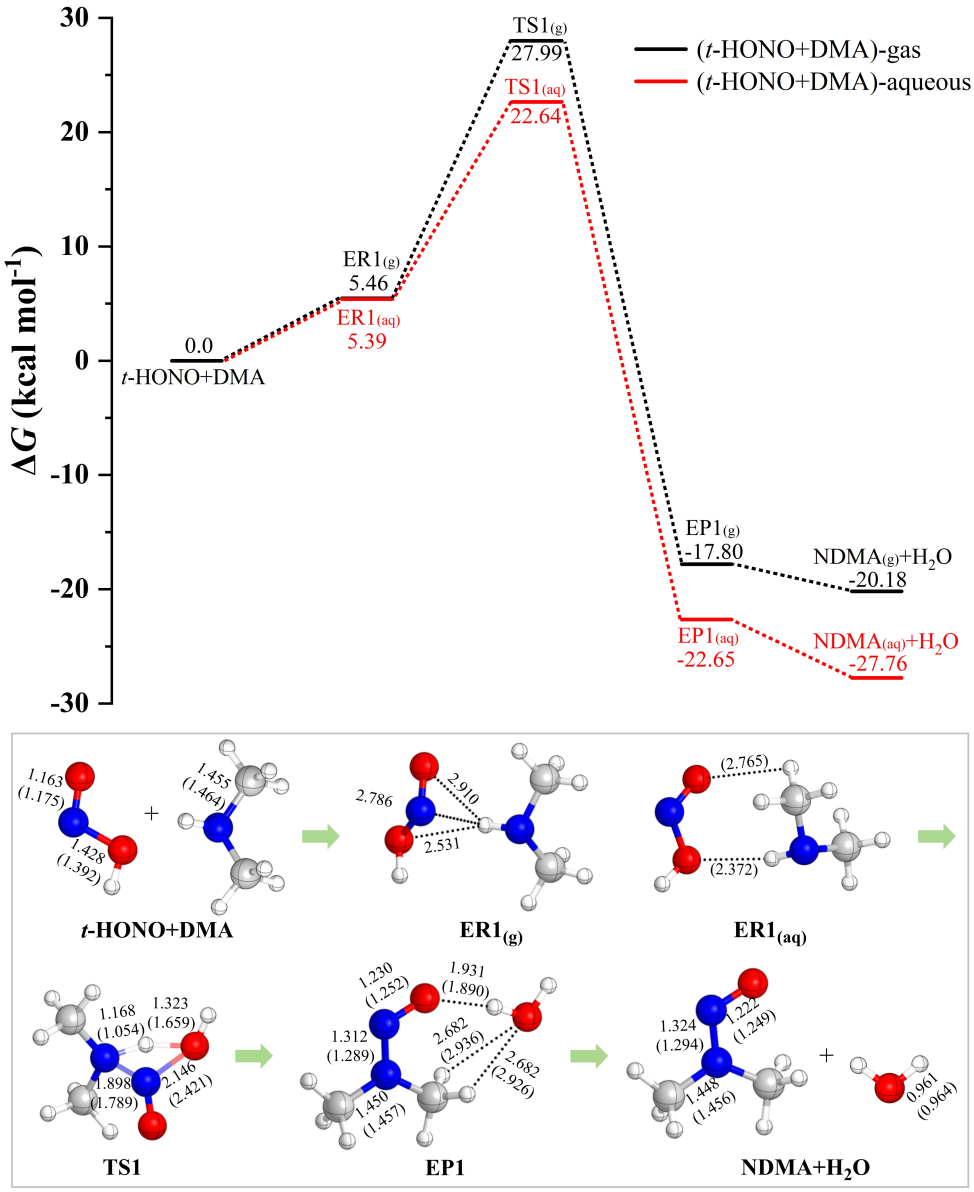

Figure S12. Potential energy surface for the reaction of *t*-HONO with DMA (unit: kcal mol^{-1}) at the CCSD(T)/aug-cc-pVTZ//B3LYP-D3/6-311++G(3df,2p) level of theory in the gas phase (g) and aqueous phase (aq). The data in parentheses are the corresponding bond lengths in the aqueous solution. The bond lengths are in angstroms (Å). The red, blue, white, and silver spheres represent O, N, H and C atoms, respectively.

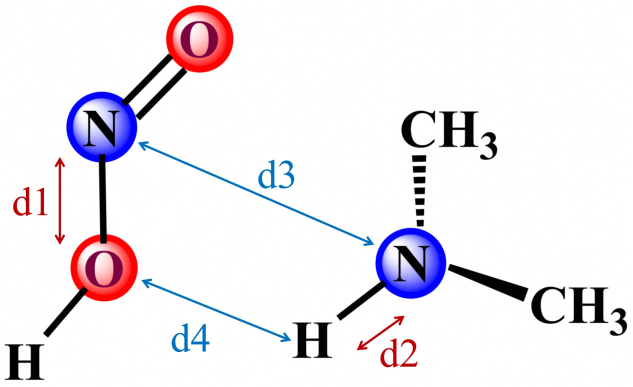

$$d_{cv} = d1 + d2 - d3 - d4$$

Figure S13. Collective variable (CV) for the metadynamics (MetaD) simulations. The CV tracks the formation (blue) and breaking (red) of all relevant bonds occurring during the N-nitrosation reaction of DMA with HONO at the air–water interface. For MetaD simulations, the CV was defined as: d_{CV} = d1 + d2 − d3 − d4.

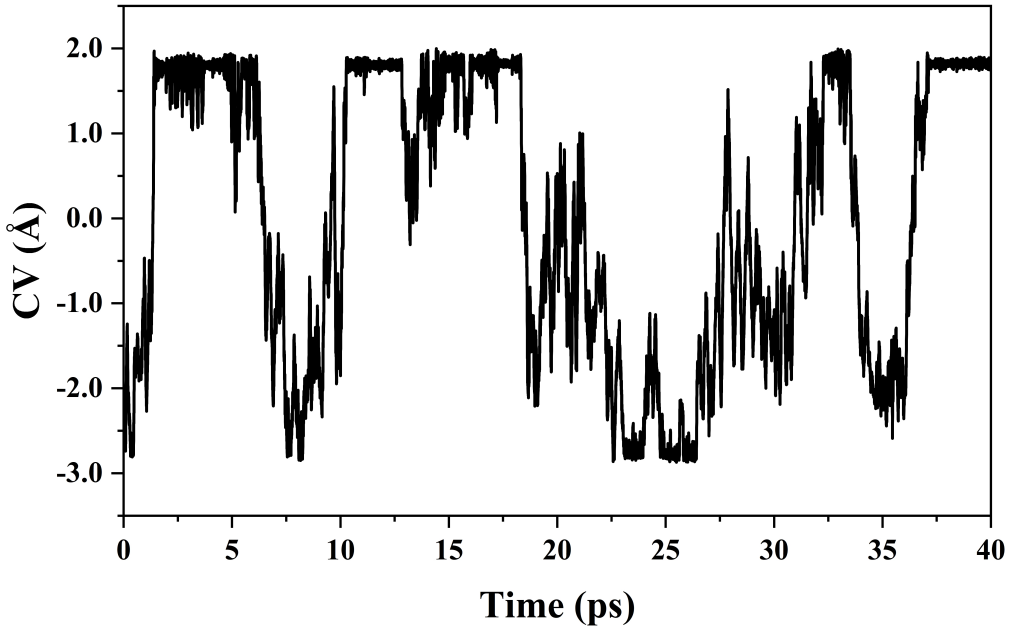

Figure S14. Convergence analysis of MetaD simulations for the N-nitrosation reaction between DMA and HONO at the air–water interface, based on the time evolution of the CV.

Table S1. Calculated frequencies (cm^{-1}) of the reactants, products, transition states and complexes at the B3LYP-D3/6-311++G(3df,2p) level of theory (g: gas phase; aq: aqueous phase simulated with the SMD model).

t-$ONONO_2$ (g)	23.35, 126.95, 211.30, 294.94, 486.98, 644.61, 780.77, 803.65, 942.03, 1328.01, 1706.49, 1937.10
t-HONO (g)	586.68, 620.05, 818.25, 1300.83, 1783.54, 3771.31
t-HONO (aq)	626.97, 645.81, 837.05, 1326.30, 1712.20, 3720.63
DMA (g)	232.64, 271.48, 396.04, 761.38, 938.66, 1040.77, 1104.09, 1165.92, 1187.95, 1268.22, 1446.89, 1473.71, 1475.79, 1489.64, 1499.46, 1516.76, 1517.32, 2918.95, 2922.30, 3037.37, 3038.03, 3085.42, 3085.92, 3529.61
DMA (aq)	225.09, 278.86, 411.48, 816.34, 938.20, 1032.33, 1096.39, 1149.48, 1204.08, 1267.05, 1445.75, 1449.81, 1467.44, 1477.11, 1490.22, 1503.47, 1503.66, 2958.66, 2958.72, 3055.49, 3057.23, 3099.86, 3100.27, 3497.63
ER1 (g)	22.53, 44.19, 56.62, 70.88, 97.59, 143.46, 233.33, 278.92, 401.76, 570.21, 606.78, 782.34, 820.99, 944.63, 1044.46, 1104.76, 1165.33, 1190.04, 1269.34, 1298.15, 1448.09, 1474.51, 1480.36, 1492.01, 1500.73, 1517.74, 1522.19, 1779.65, 2924.34, 2928.43, 3036.47, 3039.36, 3081.55, 3093.34, 3528.71, 3774.16
ER1 (aq)	30.85, 47.79, 55.46, 83.79, 95.35, 99.07, 240.06, 289.52, 412.96, 616.88, 643.18, 833.47, 838.82, 944.56, 1036.57, 1098.47, 1151.42, 1205.92, 1269.43, 1329.11, 1447.08, 1466.80, 1469.27, 1478.95, 1491.47, 1503.51, 1507.73, 1716.71, 2956.01, 2961.28, 3053.98, 3055.80, 3098.57, 3100.18, 3509.27, 3721.04
TS1 (g)	923.88*i*, 72.42, 112.27, 173.02, 218.79, 243.08, 264.83, 329.52, 378.70, 419.30, 518.08, 546.02, 654.85, 676.25, 947.38, 1074.55, 1096.70, 1173.63, 1220.53, 1267.18, 1444.70, 1462.41, 1481.46, 1490.54, 1498.59, 1505.13, 1680.97, 1715.83, 1853.83, 2988.82, 2995.37, 3038.56, 3049.83, 3066.36, 3091.17, 3848.43
TS1 (aq)	150.02*i*, 65.26, 142.93, 177.01, 218.02, 239.48, 259.54, 271.44, 304.51, 392.29, 410.16, 443.33, 675.94, 888.02, 1011.56, 1059.31, 1085.48, 1187.70, 1197.16, 1253.27, 1443.38, 1460.13, 1469.79, 1474.28, 1487.97, 1488.41, 1562.33, 1807.07, 2799.46, 3039.72, 3043.95, 3111.69, 3112.60, 3133.31, 3134.68, 3818.16
EP1 (g)	10.49, 101.43, 128.13, 151.05, 155.93, 201.02, 241.03, 345.42, 382.03, 416.06, 417.99, 555.41, 695.81, 852.49, 1061.82, 1072.31, 1106.87, 1160.94, 1316.97, 1353.72, 1441.28, 1458.19, 1480.56, 1488.33, 1496.18, 1515.58, 1521.83, 1661.00, 3022.80, 3047.48, 3076.32, 3108.92, 3139.69, 3147.03, 3685.04, 3897.52
EP1 (aq)	31.42, 87.59, 110.22, 152.78, 174.74, 211.60, 270.22, 350.80, 398.11, 419.77, 435.06, 527.74, 688.48, 850.84, 1065.35, 1103.74,

	1112.07, 1170.74, 1296.93, 1354.69, 1414.87, 1442.99, 1468.95, 1469.13, 1471.12, 1489.36, 1517.94, 1624.20, 3050.58, 3056.51, 3117.19, 3121.40, 3160.67, 3171.89, 3602.22, 3843.17
NDMA (g)	86.42, 165.93, 226.04, 338.24, 399.87, 408.38, 693.84, 856.65, 1043.18, 1063.57, 1116.95, 1162.01, 1311.98, 1341.98, 1438.84, 1457.89, 1470.69, 1487.10, 1504.56, 1517.55, 1532.49, 3015.93, 3035.95, 3066.38, 3089.70, 3133.20, 3139.10
NDMA (aq)	146.93, 184.61, 256.70, 348.82, 410.84, 428.33, 690.86, 853.11, 1061.82, 1093.57, 1111.87, 1170.50, 1298.93, 1350.58, 1416.35, 1440.65, 1463.69, 1467.91, 1468.42, 1486.64, 1514.13, 3048.32, 3053.10, 3113.00, 3114.77, 3157.38, 3168.54
H_2O (g)	1625.91, 3822.78, 3927.10
H_2O (aq)	1594.65, 3786.38, 3869.70

Supplementary Reference

Lu, T. and Chen, Q.: Interaction Region Indicator: A Simple Real Space Function Clearly Revealing Both Chemical Bonds and Weak Interactions**, Chemistry Methods, 1, 231–239, https://doi.org/10.1002/cmtd.202100007, 2021.

Mayer, I.: Charge, bond order and valence in the AB initio SCF theory, Chemical Physics Letters, 97, 270–274, https://doi.org/10.1016/0009-2614(83)80005-0, 1983.

Ning, A., Li, J., Du, L., Yang, X., Liu, J., Yang, Z., Zhong, J., Saiz-Lopez, A., Liu, L., Francisco, J. S., and Zhang, X.: Heterogenous Chemistry of I2O3 as a Critical Step in Iodine Cycling, J. Am. Chem. Soc., 146, 33229–33238, https://doi.org/10.1021/jacs.4c13060, 2024.